Impact of gold ions on nanohardness and various characteristics of G-metal alloy surface

Qaneeta Younas[1,2]*, Khurram Siraj[1], Thomas Osipowicz[2], Samia Naeem[3], Yakai Zhao[4], Cheng Cheh Tan[4], Shazia Bashir[5], Tanveer Ashraf[6], Saba Mushtaq[1], Muhammad Shahzad Abdul Rahim[1], Muhammad Mustafa Dastageer[1], Breara Muhammad Hussain[1]

[1] Laser and Optronics Centre, Department of Physics, University of Engineering and Technology, Lahore, Pakistan
[2]Centre for Ion Beam Applications (CIBA), Department of Physics, National University of Singapore (NUS), 117542 Singapore
[3] Department of Physics, Government College Women University Sialkot, Pakistan
[4] Institute of Materials Research and Engineering (IMRE), Agency for Science, Technology and Research (ASTAR), 138634 Singapore
[5] Centre for Advanced Studies in Physics, Government College University, Lahore, Pakistan
[6] Institute of Engineering and Applied Sciences, National Institute of Laser and Optronics College, Islamabad, 45650 Pakistan
*Corresponding author. E-mail address: qaneetayounas@gmail.com

Abstract

Mechanically polished Gun-metal (G-metal) alloy specimens were irradiated using a 2 MeV Au^+ beam of Pelletron Linear Accelerator. The range of Au^+ fluence was 5×10^{11} to 1×10^{14} Au^+/cm^2. XRD patterns revealed the crystallographic peaks of Cu, Zn, and Sn. Harris analysis demonstrated that the Au^+ fluence strongly influenced the preference of crystal plane alignment. The structural attributes like crystallite size, strain, etc. change as the Au^+ fluence varies. Due to the low depth of ion-induced defects region, the estimation of ion irradiated material surface hardening is difficult. So, the technique of nanoindentation used in this work proves helpful for estimating the surface hardness of ion irradiated material. The surface hardness of specimens varied with the Au^+ fluence and indentation depth. A significant increase in surface roughness, nanoindentation surface hardness, and elastic modulus values was observed at 5×10^{13} Au^+/cm^2 irradiation. Moreover, the surface hardness improves with decreasing crystallite size, reflecting the Hall-Petch relation. EDX and Proton-induced X-ray emission (PIXE) were used for elemental analysis of specimens before and after Au^+ irradiation.

Keywords: XRD; Harris analysis; Nanoindentation; FESEM; Surface roughness; PIXE; EDX

1 Introduction

Gunmetal is a Cu-Sn-Zn alloy that is used for parts including bearings, gears, valve seats, couplings, and bushings in different industrial equipment and machinery. It is appropriate for intensive use due to its strength, corrosion, and wear resistance. It can be molded into different precise parts, like shafts, gears, fittings, and bushings, used in the manufacturing and engineering sectors. Because of its strength, gunmetal can make handgun parts including barrels, and receivers. It is utilized to manufacture artillery pieces, cannons, and various other ordnances because it can

tolerate high pressure and corrosion [1-3]. Its properties especially hardness can be enhanced by ion beam irradiation. Ion beam technology is an effective and reliable method for modifying the surface properties of metal alloys through ion metal interaction. It is mostly used for material modification, lifetime tuning, and tailoring the properties of materials. The more notable features of such a technique are the high adhesion power between the bulk and modified material layer, and the great degree of control on material quality [4-6]. Many literature is found on properties modification of different materials by ion irradiation but no study is found yet on G-metal alloy properties modification by this technique. Therefore it is interesting and important to study the modification of G-metal alloy surface characteristics and its causes, upon ion irradiation.

Zhang et al., [7] elaborated the surface-morphology and microstructures of metallic alloy glasses such as Fe-Si-B and Fe-Zr-B and compared with tungsten before and just after the bombardment via He ions of energy 300 keV. The XRD results revealed that metallic glass alloy i.e., Fe-Zr-B remained amorphous following bombardment. At 4×10^{17} ions/cm^2 fluence, a modest number of beta-Mn phase nanocrystals produced in Fe-Si-B type metallic glass. When fluence grew even more, then there is increased number of nanocrystals. Cracks and blisters observed by SEM on the tungsten surface at 1×10^{18} ions/cm^2, whereas spalling and cracks emerged on the substrates of glasses whenever the fluence was increased to 1.6×10^{18} ions/cm^2.

Waseem et al., [8] analyzed the tungsten-based alloy $W_{0.5}$ $(TaTiVCr)_{0.5}$ irradiated by 200 keV helium ions to a maximal fluence of 1×10^{21} He^+ /cm^2 . Subsequently the irradiation of ions, the nanoindentation analysis revealed the magnification in hardness of the polished sample through 11.6 to 14.9 GPa at about 200nm depth. Microstructure of the treated sample analysis via transmission and scanning electron-microscope (TEM, SEM) exposed the dislocations, a few randomly black dispersed precursors, and spots of helium bubbles which caused the modification in material hardness.

Ueyama et al., [9] studied the microstructures and Vickers hardness analysis of metal alloys (CuTi) which were bombarded by Al ions (5.4 MeV), Fe ions (7.3 MeV), I ions (10 MeV), and Au ions (16 MeV) at ambient temperature. At low fluence values, the hardness was initially increased but it subsequently remained unchanged even when the ion fluence was increased. By elastic collision, deposition of energy density was strongly associated with the shift in hardness rather than electronic excitation. Atomic probe-tomography analysis revealed zero clusters of titanium in the exposed region of samples. Consequently, lattice defects (vacancies, interstitial atoms) rather than Ti-clusters were responsible for the elevation in hardening. Such alloys have received great attention in the electronic field.

Zuo et al., [10] irradiated the Ti (Ti–6Al–4V) alloy specimens with simulated nitrogen and hydrogen ion beams. XRD, SEM and TEM are used to characterize the microstructures of titanium alloy just before and afore irradiation. Large cycle fatigue and tensile characteristics of the irradiated and un-irradiated alloys were investigated. The results reveal that following irradiation through H ions, the mechanical (fatigue, tensile) characteristics decline to a greater extent than after bombardment through N ions due to the brittleness caused by the two time actions of finer grains and Ti-H.

Yang et al., [11] inspected the irradiation induced hardening of Vanadium and its alloy (V5Cr5Ti) using several ion irradiation (helium and heavy ions) at various fluence. The modification in hardness induced via ion bombardment was measured using nanoindentation. Compared to high-

energy ion irradiation, He ion beam irradiation caused a more substantial hardness both in pure Vanadium and alloy, which was attributed toward the coarsening of dislocated loops owing to the presence of He atom in the lattice. At a damage level of 0.5 dpa, TEM indicates the production of He bubbles in alloy. Because of the size constraint, He bubbles seemed to be weak impediments, according to the dispersing barrier hardening concept.

The microstructural characteristics of Aluminum (Al) bombarded with He^+ ions (18 MeV) under vacuum condition at fluence rate about 1×10^{13} to 10^{16} (ions/cm^2) were explored by Chae et al., [12]. At several irradiation fluence levels, FE-SEM data demonstrate that helium ions bombardment produces noticeable impacts in terms of pores, pits, holes, and disordered structures. These defects were distributed randomly all around the specimen surface at lower ranges of fluence such as $1 \times 10^{13} - 1 \times 10^{16}$ ions cm^{-2}, however at high fluence values (1×10^{16} He^+/cm^2) such defects density was considerably increased in terms of clusters just on the specimen surface. The XRD analysis revealed that irradiating Al with He ions beam has no result in the formation of a new phase. The shift in FWHM and intensities of diffracting plane, however suggested structural disturbance in Al lattice structure. Ions-irradiation damage profile and composition of the target specimen were also computed by SRIM code and EDS respectively.

The different ion species were employed in the above literature available research work to modify the characteristics of metal alloys. But to the best of our comprehension the Au ion (196 amu) beam is not yet used to modify the surface properties of G-metal alloy meanwhile it has many applications in different fields [3, 13]. It has also been observed that little characterization work is found by nanoindentation, especially on ion irradiated G-metal alloy specimens. Moreover, it is an advanced characterization technique. So this prompted us to investigate the impact of higher atomic mass Au ions with energy 2 MeV on the G-metal alloy samples. So five G-metal alloy samples were prepared for irradiation at different ion fluence. Later, their surface roughness, crystal structure, texture coefficient, surface composition, and nanohardness behavior were studied.

2 Experimentation

Five G-metal alloy disc shaped (radius: 8mm, thickness: 2mm) specimens were trimmed from as received rod. These samples were grinded using SiC papers upto grit 2000, polished using diamond pastes and finally cleaned ultrasonically in acetone. Four specimens were picked to get 2 MeV gold ion irradiation using Pelletron Linear Accelerator (6SDH-2- NEC USA) installed at Centre for Advanced Studies in Physics (CASP), Govt. College University, Lahore-Pakistan, while the other one was kept unirradiated for comparison. Every specimen was mounted on a sample holder using conductive double sided carbon tape inside the stainless steel chamber operating at pressure of 10^{-2} mbar. Later, the main beam line pressure valve was gradually opened to preserve a consistent base pressure of about 10^{-6} mbar within the chamber prior to irradiation. An ion beam (spot size ~ 1×1 cm^2) hit the specimen at a 90^o to the surface, and one by one specimen was irradiated with fluences of 5×10^{11}, 1×10^{12}, 5×10^{13}, and 1×10^{14} Au ions/cm^2 under identical irradiation manipulates. Throughout the experiment, beam current was measured as well using Faraday cup and recorded about 100 nA and beam average temperature was 110 °C.

To look the influence of Au^+ irradiation on specimens structural as well as mechanical characteristics, a variety of techniques are used to carry out characterization process. Ahead of ion irradiation, it is better to simulate the material and process parameters using codes such as

SRIM/TRIM codes to work systematically and prevent material wastage. The 2013 SRIM programme was implemented for the simulation of ion irradiation induced damage on the specimens surface. The numerous microstructural variables for specimens were identified employing X-ray diffractometer with specifications (Bruker, D8-Discover, Germany) Cu-K_α, λ = 0.154 nm, voltage 40 kV, and step size 0.02°. The range of 2θ was kept 30° to 100°. The specimens 3D micrographs were taken from FE-SEM (Tescan Maia-3) results and used further to investigate the surface roughness of pre and post Au^+ irradiated G-metal alloy samples using WS × M Nanotech software (5.0 develop 10.3).

Nanoindentation (Nanoindenter, G200, KLA) tests with Berkovich indenter tip were performed to examine the role of ion irradiation on the specimens hardness. The indentation load-depth profiles were obtained using continuous-stiffness measurement (CSM) mode [14, 15]. A maximum depth of 2000 nm was applied at an indentation strain rate of 0.025 s^{-1} [16, 17], and five indentations were conducted for each condition to ensure reproducibility.

When ion irradiation is used to modify the material surface properties, then certain ions can be immersed inside the material instead of just colliding with atoms on the surface and change its crystal structure, elemental makeup, etc. So, Energy dispersive X-ray (EDX) spectrometer and Proton-induced X-ray emission (PIXE) technology were used to identify the elemental makeup of pristine and Au^+ irradiated G-metal alloy specimens [18, 19]. A 3.5 MeV Singletron accelerator at the Center for ion beam applications (CIBA), department of physics, National University of Singapore (NUS), was used to generate a 2 MeV proton beam for PIXE analysis. The OMDAQ-3 software was used to process the collected X-ray spectra offline.

3 Results and discussion

3.1 SRIM contemplated damage profiles

When high-energy ions interact with metals then lattice atoms are displaced from their locations, which are mostly associated with the ion energies. Ions that have been bombarded drop their energies when they collide with metal atoms or electrons in elastic or inelastic collisions. In fact, the kind of ion and the atomic structure of the targeted substance have a significant impact on the penetration depth of such energetic ions [12]. Additionally, the dislocation of lattice atoms from their positions is caused by the decrease in ion energy following the collisional processes of electronic (S_e) and nuclear (S_n) stopping powers. The target material experiences the lattice atoms displacement upon ion irradiation, which also causes point imperfections i.e. interstitials and vacancies. When dealing with highly energetic but less massive ions, the S_e mechanism stands out as the more dominant of the two. Conversely, the S_n mechanism is more pronounced for high-energy and massive ions. So, to analyze the intricate damage profile resulting from the irradiation of G-metal alloy with 2 MeV Au^+, SRIM-2013 software [20] was employed. This software computed a range of parameters including the total displacements, anticipated ion range, ion distribution, electronic (S_e) and nuclear stopping (S_n) powers, and ion straggling. The 2D longitudinal and transverse views, 3D damage plot, and ion distribution for 2 MeV Au^+ irradiation of G-metal alloy specimens were illustrated in Fig. 1a-d. According to the simulation results, the Au^+ average projectile range (R_p) is ~0.18 μm, whereas the other parameters like longitudinal straggling, lateral straggling, S_e, and S_n have approximate values of 424 Å, 334 Å, 3.26 keV/μm, and 8.15 keV/μm, respectively. The incoming ions induce electronic excitation, vacancies, and

interstitials along the direction of their motion which may lead to longitudinal and lateral damages [12].

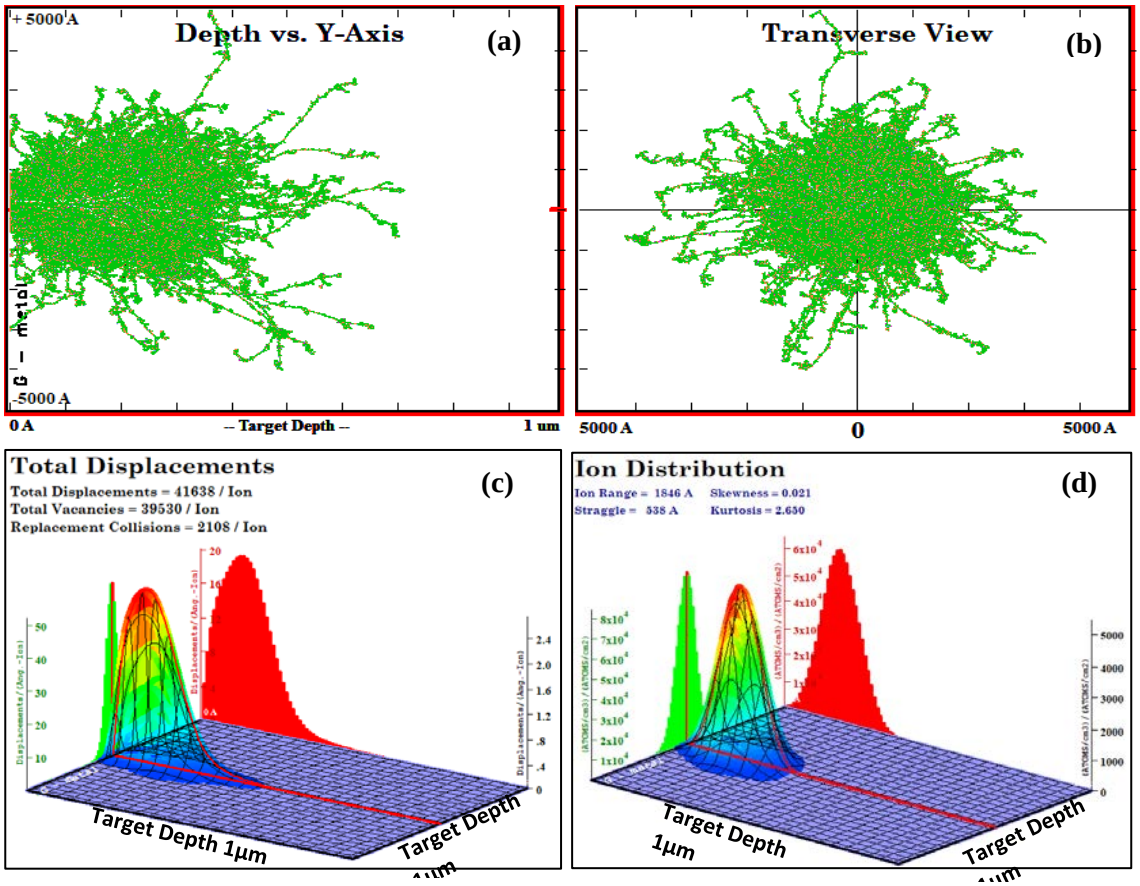

Fig. 1 Irradiation of G-metal alloy with 2 MeV Au^+ **(a)** 2D longitudinal view **(b)** 2D transverse view **(c)** 3D damage plot and **(d)** 3D ion distribution plot by SRIM simulations

3.2 XRD characterization

XRD plots of pristine (G0) and Au^+ irradiated G-metal alloy specimens with fluences of 5×10^{11} (G1), 1×10^{12} (G2), 5×10^{13} (G3) and 1×10^{14} (G4) Au^+/cm^2 are depicted in Fig. 2a. All the observable crystallography peaks have been identified on comparing with the standard- reference patterns of Cu (JCPDS: 00-004-0836), Sn (00-004-0673), and Zn (00-004-0831). The Au^+ irradiated G-metal alloy specimens demonstrate several planes i.e. (101), (002), (111), (200), (102), (400), (220), and (311) consecutively, which are identical to those in the pristine specimen.
However referring to Fig. 2a, as increasing ion fluence from G0 to G4 specimens, the diffracted peaks shifting (2θ), intensity (I) adaptations, and FWHM of the samples are found to be altered unevenly. This indicates that Au^+ irradiation induced imperfections and strain in the material lattice structure [8]. Table 1 lists several details about four more noticeable planes namely (111), (200), (220), and (311) of Cu-metal, i.e. the basic metal of G-metal alloy. The Gaussian function is applied to the actual data of a specific peak in order to precisely determine the peak position (2θ/degree), peak intensity, and FWHM. The diffracted peaks FWHM (β) data is determined using this relation: $\beta = (2\ln 2)^{1/2} w = 1.1774w$ [7].

For further justification Cu (111) is considered in Fig. 2b, that reveals the peak intensity of the considered plane is increased significantly at ion fluence 5×10^{11} Au^+/cm^2 and afterward decreases with further increasing the ions fluence upto 1×10^{14} Au^+/cm^2. Makinson et al. provide the physical consequences of the rise or fall in the peaks intensity values. Their computational studies demonstrated that the density of induced point defects (dislocation density) within a material influence the x-ray diffracted peaks intensity. The peak-intensity (*I*) rises when induced point defects (like vacancies) density falls and vice versa [21].

Fig. 3 illustrates the correlation between the Cu (111) plane diffracted peak intensity and FWHM values as a function of Au^+ fluence. It is observed that both parameter values vary oppositely with the Au^+ fluence. This could be justified by Ungars studies [21], which revealed that x-ray diffracted peak is widened if lattice imperfections including point defects, vacancies, etc. are greatly increased. Consequently, a decline in the plane peak intensity due to a rise in defect concentration is associated with peak broadening.

The shifting in Cu (111) peak position as a result of variations in Au^+ fluence is also depicted in Fig. 2b. It can be noticed from G1 to G4 that when the G-metal alloy is exposed to Au^+, the diffracted Cu (111) peak is little displaced towards the lower angles w.r.t. G0 (see Table 1). The peak position shifting towards a lower angle value indicates that a tensile strain is induced in the specimen upon ion irradiation [12].

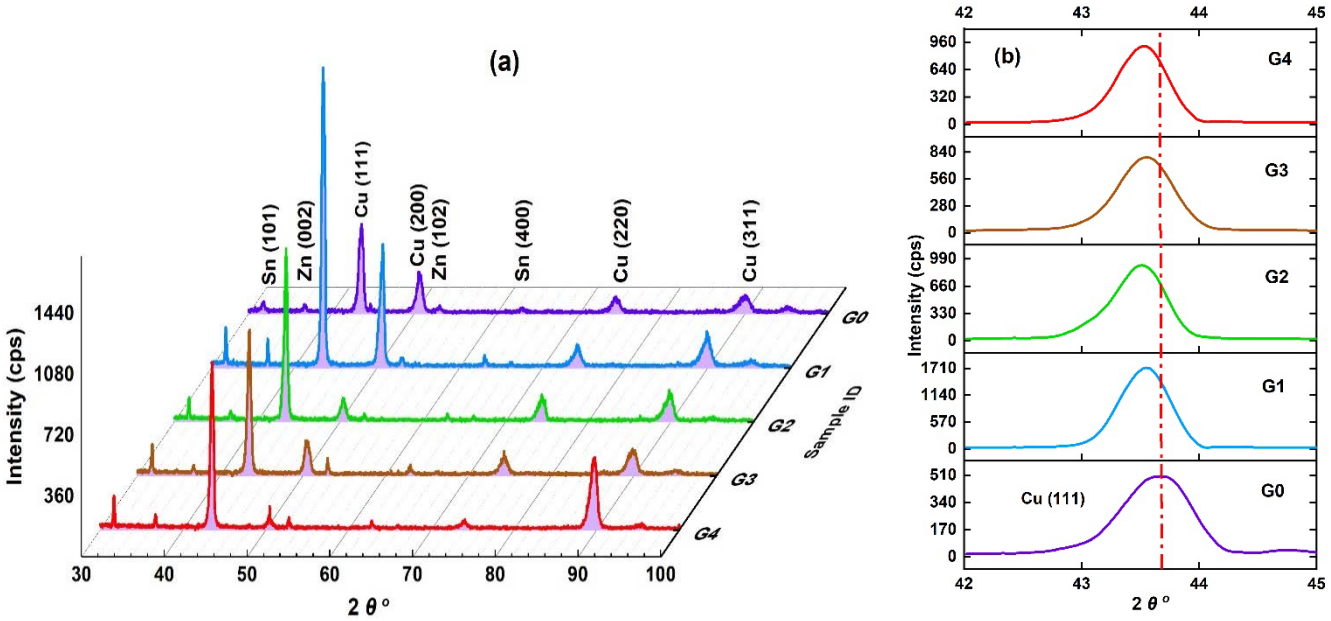

Fig. 2 (a) X-ray diffraction 3-D pattern of pristine and Au^+ irradiated G-metal alloy specimens and **(b)** comparison of Cu (111) peak adaptations and shifting

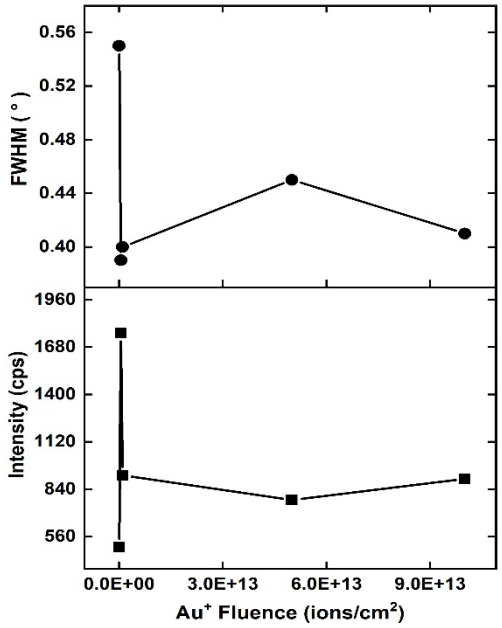

Fig. 3 FWHM and Intensity of Cu (111) peak for pristine and Au^+ irradiated G-metal alloy as a function of Au^+ fluence

Table 1 Parameters of the four observed diffracted peaks of pristine and Au^+ irradiated G-metal alloy

Au^+ fluence (ions/ cm^2)	Sample Identity	Parameter	Unit	(111)	(200)	(220)	(311)
0	G0	2θ	(°)	43.636	50.708	74.425	89.957
		I	(cps)	495.739	206.797	72.910	85.175
		FWHM	(°)	0.549	0.689	0.882	1.272
5×10^{11}	G1	2θ	(°)	43.538	50.632	74.243	89.857
		I	(cps)	1763.52	608.468	100.643	152.588
		FWHM	(°)	0.392	0.541	0.761	0.986
1×10^{12}	G2	2θ	(°)	43.493	50.431	74.395	89.814
		I	(cps)	921.31	109.818	121.374	138.846
		FWHM	(°)	0.395	0.595	0.858	0.972
5×10^{13}	G3	2θ	(°)	43.517	50.479	73.979	89.639
		I	(cps)	775.542	74.068	32.743	387.212
		FWHM	(°)	0.445	0.159	0.612	0.813
1×10^{14}	G4	2θ	(°)	43.542	50.545	74.338	89.823
		I	(cps)	900.84	182.699	93.310	130.936
		FWHM	(°)	0.411	0.662	0.806	1.089

3.2.1 Harris analysis

Texture, which is correlated with the crystallographic plane alignments in a polycrystalline material, may be found in nearly all manufactured or treated materials. The material quality can be strongly influenced by texture. The material is expected to be texture-free if all of the crystal planes (*hkl*) inside it are randomly aligned. Conversely, the material will possess a certain texture if the planes are aligned in a particular way. Harris analysis is carried out to determine the texture-coefficient '*P* (*hkl*)' of the target polycrystalline samples with the assistance of the given expression [22, 23]:

$$P(hkl) = \frac{I(hkl)}{I_o(hkl)}\left[\frac{1}{n}\sum_{i=1}^{n}\frac{I(h_i\,k_i\,l_i)}{I_o(h_i\,k_i\,l_i)}\right]^{-1} \quad (1)$$

Here, I_o (*hkl*) and *I* (*hkl*) denote as standard and measured relative intensity of diffraction peak respectively for a specific plane (*hkl*). '*n*' denotes the number of all the notable planes in a particular XRD pattern. For any specific plane, if term *P* (*hkl*) > 1 then such (*hkl*) plane seems to have a considerable orientation.

Applying Eq. (1) to calculate the texture coefficient of four more noticeable planes namely (111), (200), (220), and (311) by putting I_o (*hkl*) from the reference standard pattern of Cu (JCPDS: 00-004-0836) and all calculated variables are mentioned in Table 2. Fig. 4 depicts the texture-coefficients (*P*) of four prominent crystallographic (*hkl*) planes of pristine and Au^+ irradiated G-metal alloy as a function of plane position 2θ. It is apparent from Fig. 4 that the Au^+ fluence influences the '*P*' value of given planes.

Fig. 4a depicts that the (111), (200), and (220) planes have '*P*' > 1 while other plane (311) has '*P*' < 1 (Table 2), so (111), (200), and (220) are preferred oriented planes in pristine material. In 5×10^{11} Au^+/cm^2 irradiated material (Fig. 4b) the (111) and (200) planes orientation remains preferable meanwhile (220) plane gets a non-preferable orientation with (311). Furthermore, in 1×10^{12} Au^+/cm^2 irradiated G-metal alloy, the plane (311) became preferable orientation with another preferred plane (111) meanwhile (200) became non-preferable along with (220) and upto 1×10^{14} Au^+/cm^2 fluence, the material has a similar preferable orientation of planes (Fig. 4c-e). Consequently, the maximum peak intensity plane is always the preferable oriented plane (Fig. 2a) of the material but also along with it the other preferable orientation of the material is influenced by the irradiation fluence.

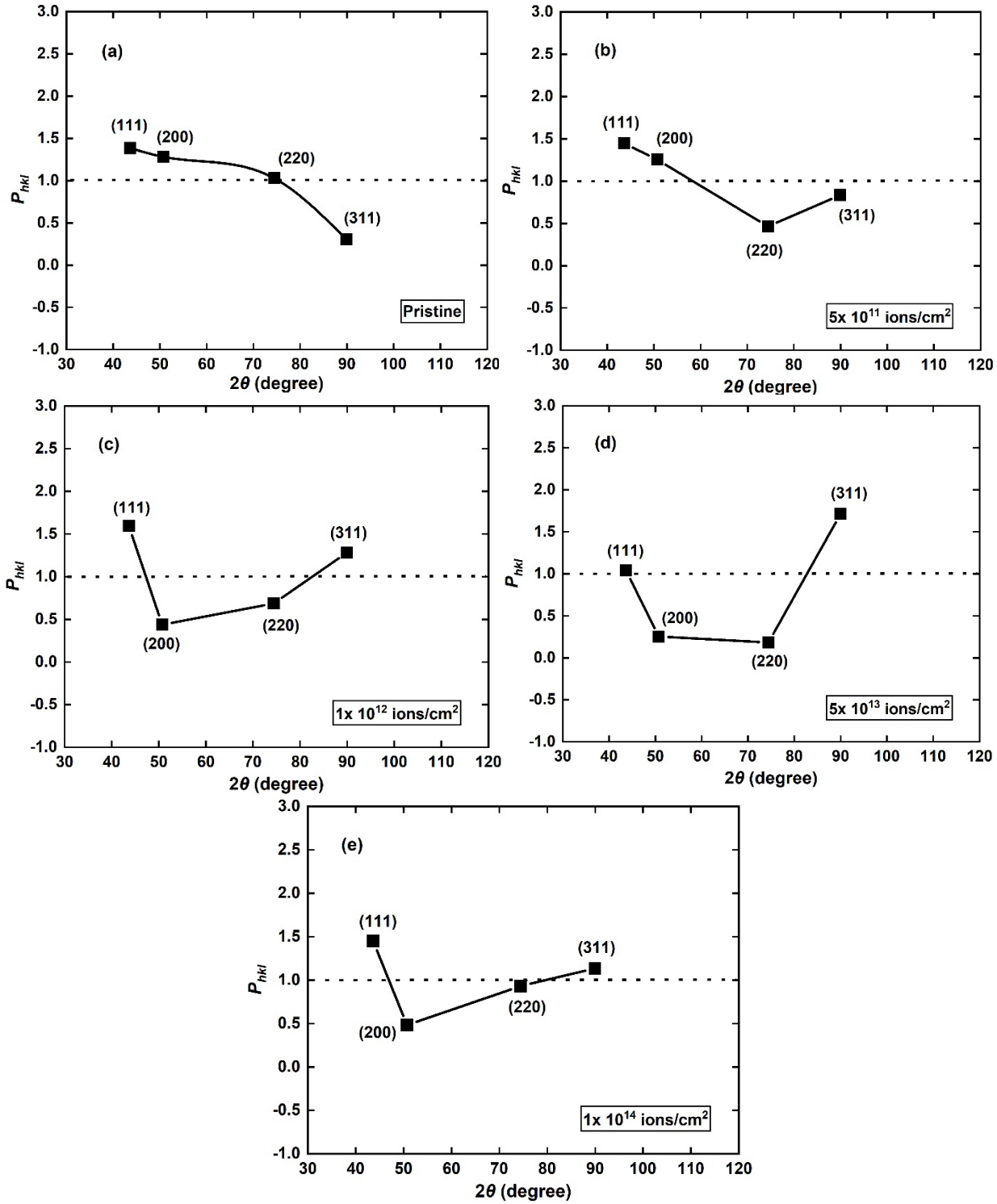

Fig. 4 Texture-coefficients (*P*) of **(a-e)** four prominent crystallographic (*hkl*) planes of pristine and Au^{+} irradiated G-metal alloy specimens

Table 2 The measured values of relative-intensity (*I*), and texture-coefficients (*P*) of four prominent crystallographic (*hkl*) planes of pristine and Au^+ irradiated G-metal alloy

(a) Measured relative-intensity *I* (%)							
2θ (°)	Plane	Standard relative-intensity I_o (%)	Measured relative-intensity *I* (%)				
			0	5×10^{11}	1×10^{12}	5×10^{13}	1×10^{14}
43.636	(111)	100	100	100	100	100	100
50.708	(200)	46	42.57	39.88	12.56	11.18	15.3
74.425	(220)	20	14.85	6.43	8.6	3.52	12.83
89.957	(311)	17	3.72	9.81	13.65	18.06	13.3
(b) Texture-coefficient *P* (*hkl*)							
2θ (°)	Plane	Standard relative-intensity I_o (%)	Texture-coefficient *P* (*hkl*)				
			0	5×10^{11}	1×10^{12}	5×10^{13}	1×10^{14}
43.636	(111)	100	1.386	1.446	1.596	1.040	1.451
50.708	(200)	46	1.282	1.254	0.436	0.253	0.482
74.425	(220)	20	1.029	0.465	0.686	0.183	0.931
89.957	(311)	17	0.303	0.835	1.282	1.712	1.135

3.2.2 Williamson-Hall analysis

Williamson-Hall analysis is employed to identify the structural characteristics like crystallite size (*D*) as well as lattice strain (ε) [24] in both pristine and Au^+ irradiated G-metal alloy. As it is considered that crystallite size and strain both are the causes of peak broadening in the resultant XRD patterns, so the W-H approach is an effective way to assess structural characteristics precisely through FWHM values of diffracted peaks. The following mathematical expression provides the FWHM (β) of a diffracted peak, expressed in radians [12, 21]:

$$\beta = \beta_D + \beta_\varepsilon \tag{2}$$

Here, crystallite size *D* and strain ε contribute significantly to the β_D and β_ε respectively. The Scherer equation relates the 'β_D' to crystallite size as follows:

$$\beta_D = \frac{k\lambda}{D\cos\theta} \tag{3}$$

The Wilson equation relates the 'β_ε' to lattice strain as follows:

$$\beta_\varepsilon = 4\varepsilon\tan\theta \tag{4}$$

Combining Eqs. (2)-(4) yields the Williamson-Hall expression:

$$\beta\cos\theta = \frac{k\lambda}{D} + 4\varepsilon\sin\theta \tag{5}$$

For simplifying the data analysis Eq. (5) can be expressed as:

$$\beta \cos\theta = A + B\ (4\ \sin\theta) \tag{6}$$

Where, $A = k\lambda/D$ and $B = \varepsilon$ are dimensionless parameters. The lattice strain and crystallite size of the sample can be estimated by plotting '4sinθ' on the x-axis and 'βcosθ' on the y-axis for every noticeable diffracted Cu-peaks. Fig. 5a-e displays the W-H plots (βcosθ versus 4sinθ) for pristine and Au^+ irradiated G-metal alloy. By using the least-square fit approach, a linear line is fitted toward data points; its intercept '*A*' value serves to calculate the crystallite size, and its slope '*B*' value is a measurement of strain (ε) in the specimen. Referring to Fig. 6a, it is observable that both the structural parameters like lattice strain and crystalline size fluctuate in approximately a similar way as a function of Au^+ fluence. As a result, it is anticipated that the relationship between '*D*' and 'ε' will be linear and Fig. 6b illustrates this by fitting the linear line to the observed data points using the least-square fitting approach. It is important to note that lattice strain positive values reveal its tensile nature [24, 25].

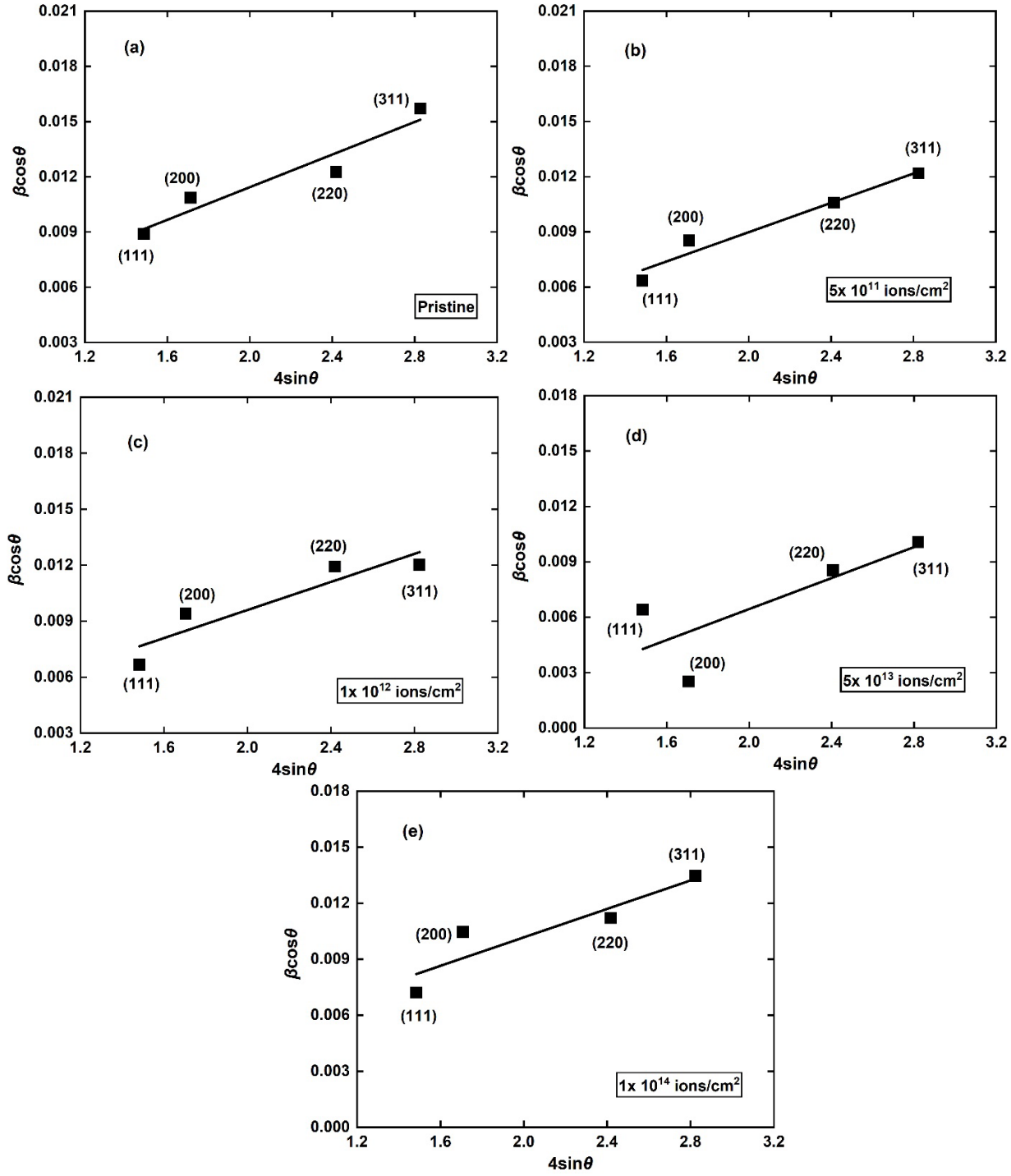

Fig. 5 Williamson – Hall (W-H) Plots (a-e) for pristine and Au^{+} irradiated G-metal alloy specimens

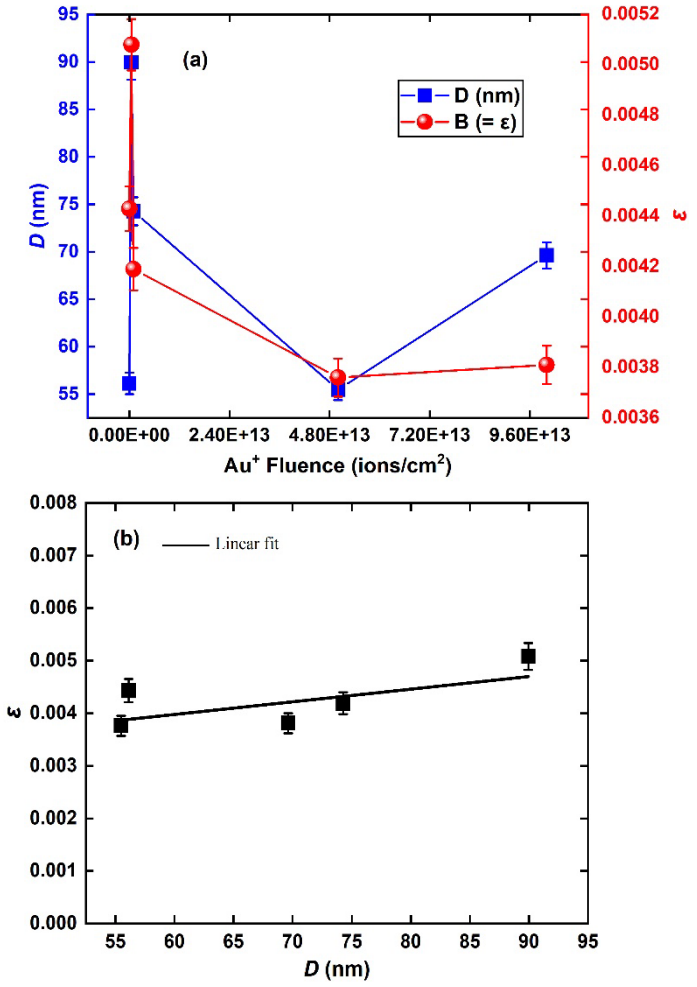

Fig. 6 (a) Plot showing crystallite size '*D*' and lattice strain '*ε*' of pristine and Au^+ irradiated G-metal alloy as a function of Au^+ Fluence, and **(b)** Correlation of '*D*' and '*ε*'

3.3 Nanoindentation-Assessed mechanical characteristics

The mechanical behavior, mainly nanoindentation hardness (*H*) and elastic modulus (*E*), of the pristine and Au^+ irradiated G-metal alloy surface were evaluated using nanoindenter. Fig. 7a depicts the indentation load versus depth curves for each specimen (G0-G4). It is noticeable that the specimens exhibit variation in indentation load even though these were subjected to the same indentation depth of 2000 nm. The Au^+ irradiation effect on *H* is also shown in Fig. 7b, which represents the averaged response of nanohardness versus depth in different specimens. Under the same maximum depths, specimen G1 (5×10^{11} Au^+ / cm^2) shows the lowest maximum indentation load (*P*) value and hence the lowest peak *H* value (at about 200 nm depth), compared to other irradiated and pristine specimens. For G3 specimen, the *H* rapidly increases and reaches a peak at about 60 nm depth. Overall, with increasing irradiation dose from 5×10^{11} to 1×10^{14} Au^+/ cm^2, the maximum hardness depth shifts from 200 nm (G1) to 60 nm (G3) and the maximum nanohardness increases from 2.24 to 3.93 GPa (Table 3).

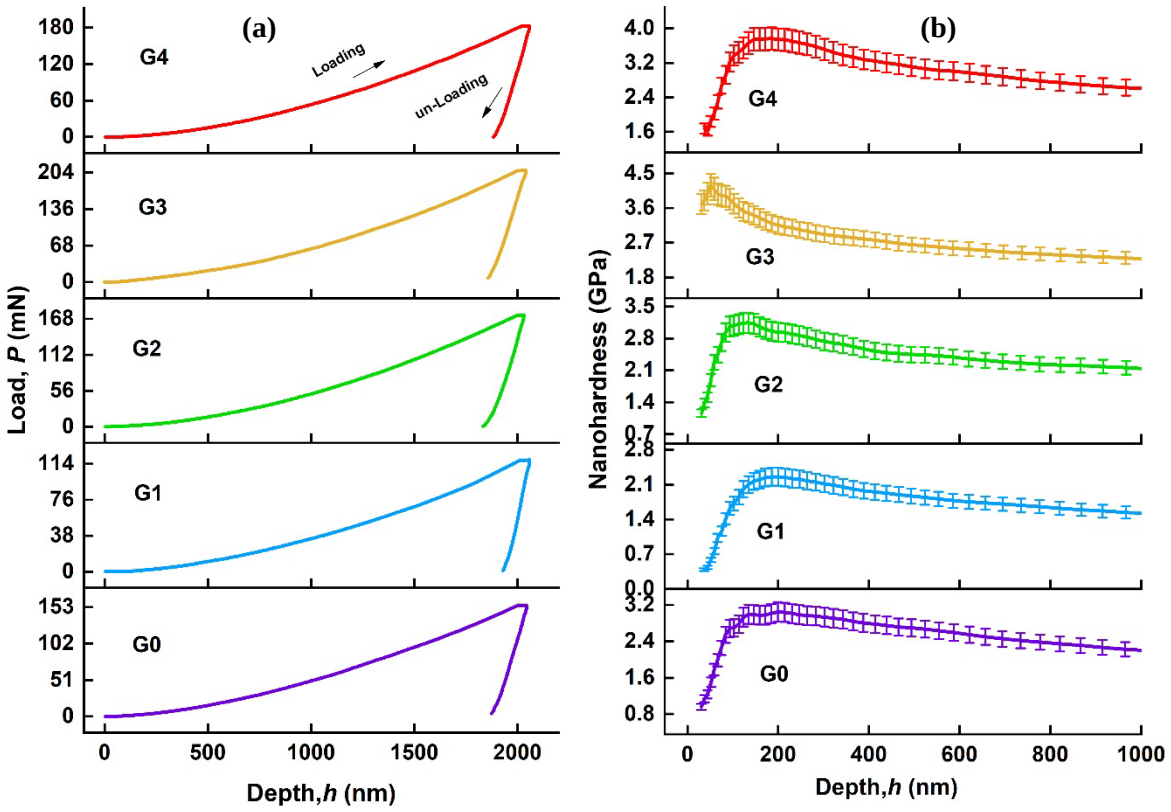

Fig. 7 Nanoindentation plots showing **(a)** indentation load versus depth curves and **(b)** nanohardness versus depth for pristine and Au^+ irradiated G-metal alloy

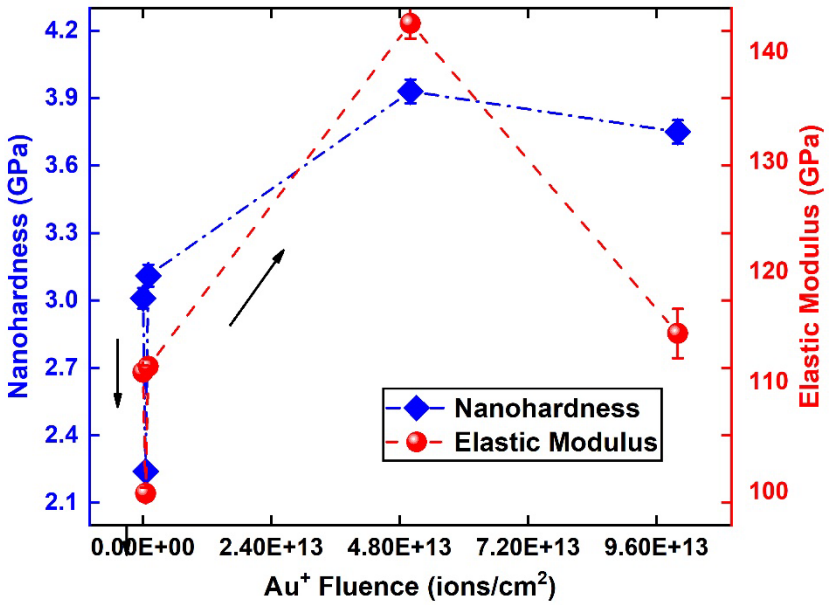

Fig. 8 Nanohardness and elastic modulus of pristine and Au^+ irradiated G-metal alloy specimens as a function of Au^+ fluence

Table 3 The average values of nanohardness and elastic modulus at depth (*h*) for pristine and Au^+ irradiated G-metal alloy specimens

Au^+ fluence (ions/ cm^2)	*h* (nm)	*H* (GPa)	*E* (GPa)
0	200	3.01	110.91
5×10^{11}	200	2.24	99.91
1×10^{12}	135	3.11	111.43
5×10^{13}	60	3.93	142.62
1×10^{14}	179	3.75	114.43

The average *H* and *E* values for each specimen are displayed in Fig. 8, and a similar fluence-dependence behavior for both was observed. The *H* and *E* results for G-metal alloy were obviously affected by the different Au^+ fluence (Table 3). Upon Au^+ irradiation, the *H* value first decreases for about 25% at lower fluence of 5×10^{11} Au^+/cm^2 (compared to that in G0 sample), and later increases and reaches 3.93 GPa up to the fluence of 5×10^{13} Au^+/cm^2 (Fig. 8) (Table 3). The Au^+ induced defects in material are usually the main cause of material hardening [26, 27]. So, the high *H* values are the further evidence of increase the defects in G-metal alloy surface, induced by the Au^+ irradiation.

3.4 FESEM analysis

FESEM micrographs in Fig. 9 portray the surface structure of G-metal alloy specimens, induced by the Au^+ irradiation. Each micrograph reveals the distinct structures that are randomly dispersed throughout the material surface. The formation of such distinct surface structures with 2 MeV Au^+ irradiation can be justified by the fact that when the energetic (2 MeV) ions interact with material then they transfer some energy by elastic (nuclear) and inelastic (electronic) collisions. The deposited energy induces the ionization and lattice atoms displacement from their original positions. Following inelastic collisions, the energetic ions shared their energy to specimen atoms via electron-phonon interaction, which generate confined heat and its shocks in the specific ions treated region. So heating (thermal spikes) and rapid cooling caused by irradiation, serve as crucial part to generate surface imperfections like distinct structures on the exposed surface [28].

Following Fig. 9b-e, the combined impact of Au^+ energy (2 MeV) and its induced heat leads to melting, and surface exfoliating, and then rapid cooling disrupt the G-metal alloy surface by creating clusters and distinct circular agglomers. When the Au^+ fluence is elevated from 5×10^{11} Au^+/cm^2 then the density and size of agglomers is raised. The incoming Au^+ leads to cluster diffusion, which is thought to be the cause of agglomer size enlargement [29]. Another interpretation is related to intensify the nucleation activity as increasing the Au^+ fluence. Consequently, the Ostwald growing mechanism occurs, wherein the low value melting point specimens atom nuclei disperse and actively contribute to the growth and enlargement of the agglomers [30]. Fig. 9e-f demonstrates robust heating with melting and then re-solidification of G-metal alloy surface during Au^+ irradiation with the highest dosage of about 5×10^{13} to 1×10^{14} Au^+/cm^2.

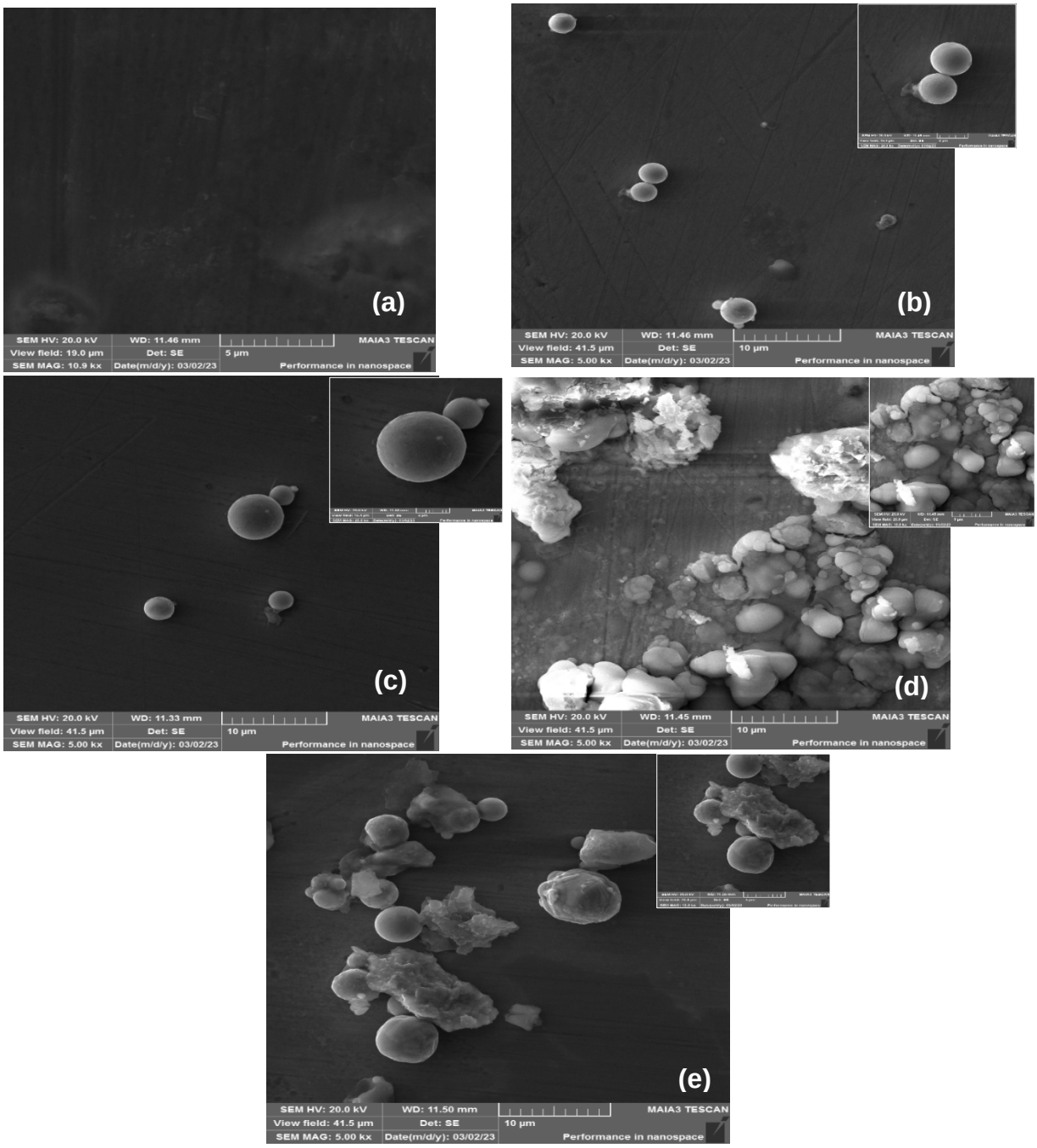

Fig. 9 FESEM micrographs of pristine and Au^+ irradiated G-metal alloy specimens: **(a)** pristine, **(b)** 5×10^{11}, **(c)** 1×10^{12}, **(d)** 5×10^{13}, and **(e)** 1×10^{14} Au^+/cm^2

3D representations of FESEM photographs and their topographic histograms in Fig. 10 are generated by applying WS × M Nanotech software (5.0 develop 10.3) [31] on FESEM micrographs (Fig. 9). The 3D photographs of specimen's surface indicate the influence of Au^+ beam irradiation on G-metal alloy surface at various fluence. X-axis of topographic histogram reflects the vertical height of measuring points as well as y-axis depicts the total number of measuring points corresponding to the specific height over the examined region of G-metal alloy. The G-metal alloy specimens surface roughness outcomes like R_A (Average) and R_{RMS} (Root- Mean-Square) are estimated by applying the WS × M Nanotech software and displayed in Table 4. The mathematical terms for R_A and R_{RMS} are expressed as [32]:

$$R_A = \left(\frac{1}{L}\right) \sum_{i=1}^{L} |N_i - N_o| \tag{7}$$

$$R_{RMS} = \left[\left(\frac{1}{L}\right) \sum_{i=1}^{L} |N_i - N_o|^2\right]^{\frac{1}{2}} \tag{8}$$

Here L = total number of measuring points over the examined region, N_i represents the magnitude of specific specimen point and N_o represents the average magnitude within the examined region. It is observed that both the surface roughness like R_A and R_{RMS} fluctuate in approximately a similar way as a function of Au^+ fluence (Table 4). Surface roughness is elevated significantly upto fluence 5×10^{13} Au^+/cm^2 and afterward decreases with further increasing the ion fluence upto 1×10^{14} Au^+/cm^2. The ion induced defects lead to an increase in the specimens surface roughness, while the resolidification of these defects helps to reduce the specimens surface roughness [32]. It explains that the overall surface roughness is influenced by many surface characteristics, such as Au^+-induced various structures (Fig. 9) and imperfections.

Table 4 The Average (R_A) and Root-Mean-Square (R_{RMS}) surface roughness values for pristine and Au^+ irradiated G-metal alloy specimens

Au^+ fluence (ions/cm^2)	R_A a.u.	R_{RMS} a.u.
Pristine	3220	5893
5×10^{11}	3421	6302
1×10^{12}	3996	6671
5×10^{13}	1039	1348
1×10^{14}	5296	7905

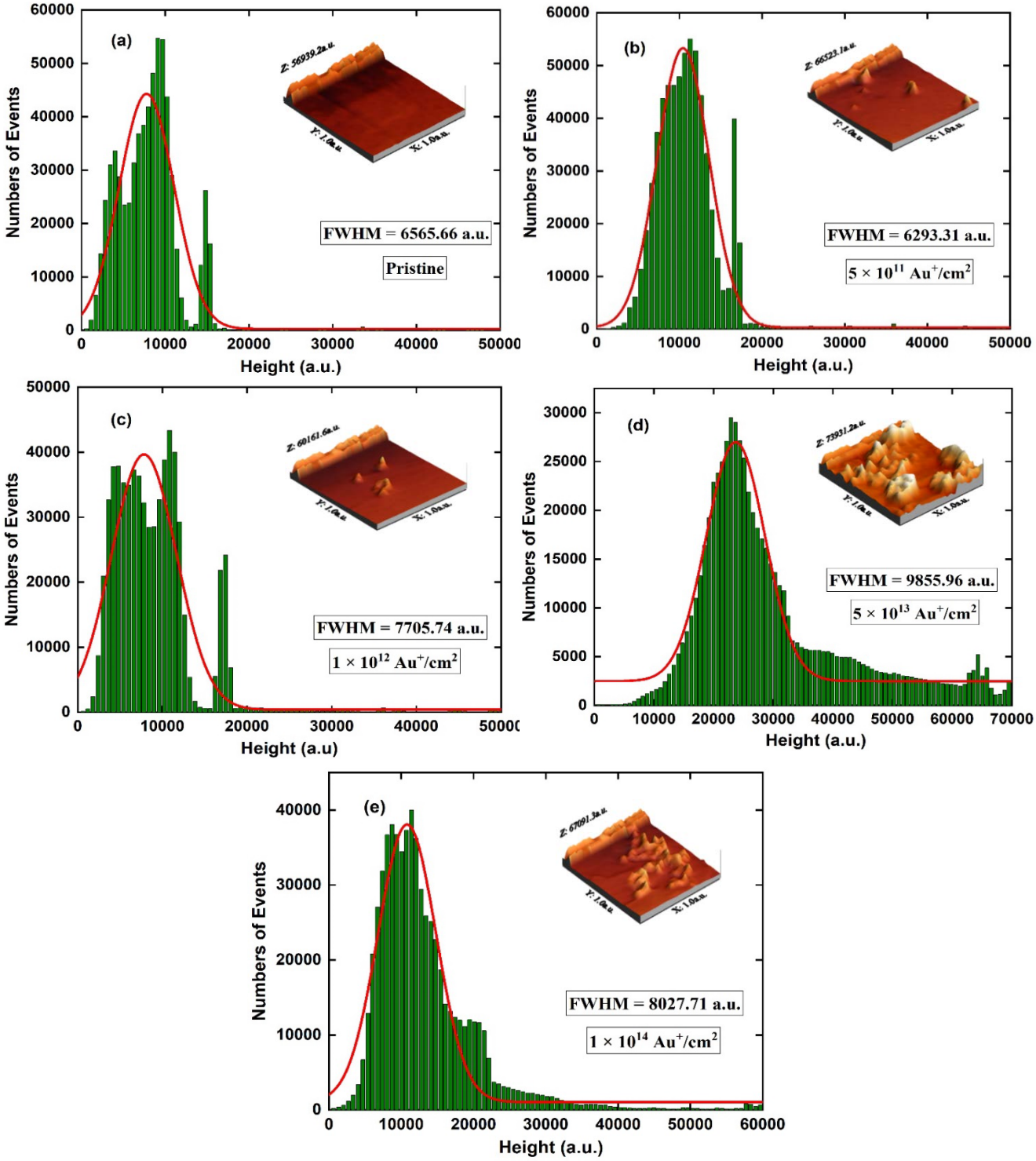

Fig. 10 FESEM 3D micrographs and topographic histograms of pristine and Au^+ irradiated G-metal alloy specimens

3.5 EDX and PIXE analysis

Fig. 11 exhibits the details of the PIXE spectrum acquired after the bombardment of a proton beam, and the EDX spectrum obtained after the bombardment of an electron beam on G-metal alloys (G0 to G4). These spectra display the multiple characteristic x-ray peaks, indicating the various elements corresponding to their energies that comprise the specimen. Using EDX and PIXE, the significant elements i.e. Cu, Zn, Sn, and Pb with K, L, and M lines (see Table 5) of specimens were identified. However, it is observed in Fig.11b that the PIXE technique did not identify the $CuL_{\beta 1}$ x-ray emission from the specimen, while it is detected by EDX (see Fig. 11a). Because in the PIXE experimental setup, the Si drift detector (SDD) is typically used to collect the emitted x-rays. The lowest value of energy that can be measured efficiently by SDD is around 1 keV [33, 34], and the $CuL_{\beta 1}$ x-ray emission has energy ~ 0.950 keV. Similarly, PbM_{α} and PbL_{α} peaks having energy ~ 2.342, and 10.550 keV respectively, are detected by PIXE but not identified by the EDX spectrometer. Because PIXE uses a high energy proton beam to ionize the atoms deeply and generates more x-rays than EDX, which leads to more precise elemental detection [35]. SRIM results (see Fig. 12) verify that the proton beam has significantly deeper penetration and a wider distribution range in G-metal alloy.

It is noticeable that the PIXE provides more distinct, sharper, and precise elemental peaks with K, L, and M lines as compared to EDX spectroscopy. The PIXE method is highly sensitive and offers fast measurements (in few minutes) due to efficient x-ray production. Additionally, less production of Bremsstrahlung radiations and smaller background noise characteristics make the PIXE more precise technique for detailed elemental analysis [36, 37].

Table 5 The list of recognized elements of G-metal alloy specimen by EDX and PIXE

Elements/lines	Energy (keV)	Techniques
$CuL_{\beta 1}$	0.950	EDX
CuK_{α}	8.040	EDX, PIXE
CuK_{β}	8.904	EDX, PIXE
SnL_{α}	3.443	EDX, PIXE
$SnL_{\beta 1}$	3.662	EDX, PIXE
$SnL_{\beta 2}$	3.904	EDX, PIXE
$SnL_{\gamma 1}$	4.130	EDX, PIXE
ZnK_{α}	8.630	EDX, PIXE
PbM_{α}	2.342	PIXE
PbL_{α}	10.550	PIXE

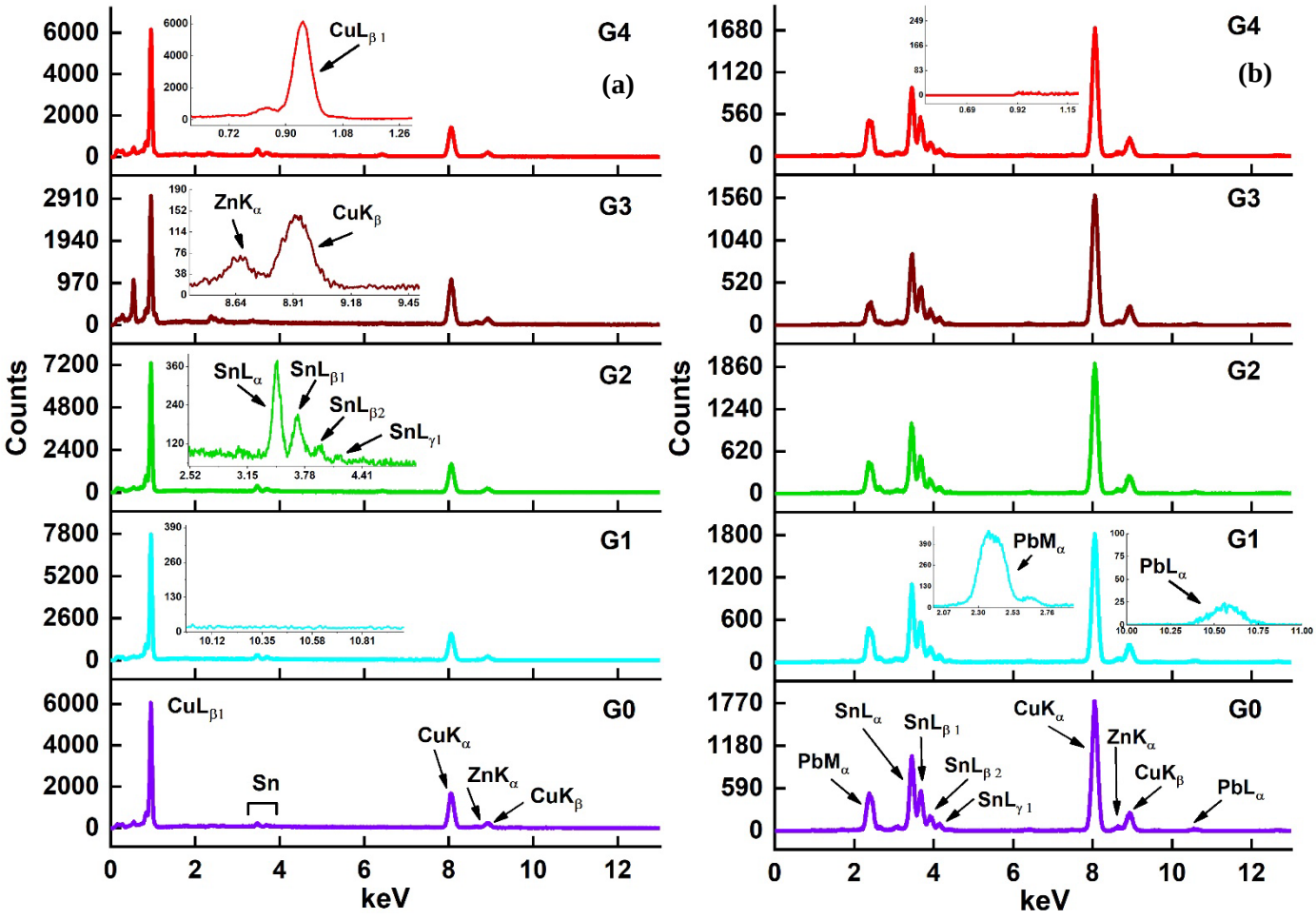

Fig. 11 Elemental peaks identification for pristine and Au^{+} irradiated G-metal alloy specimens from **(a)** EDX, and **(b)** PIXE

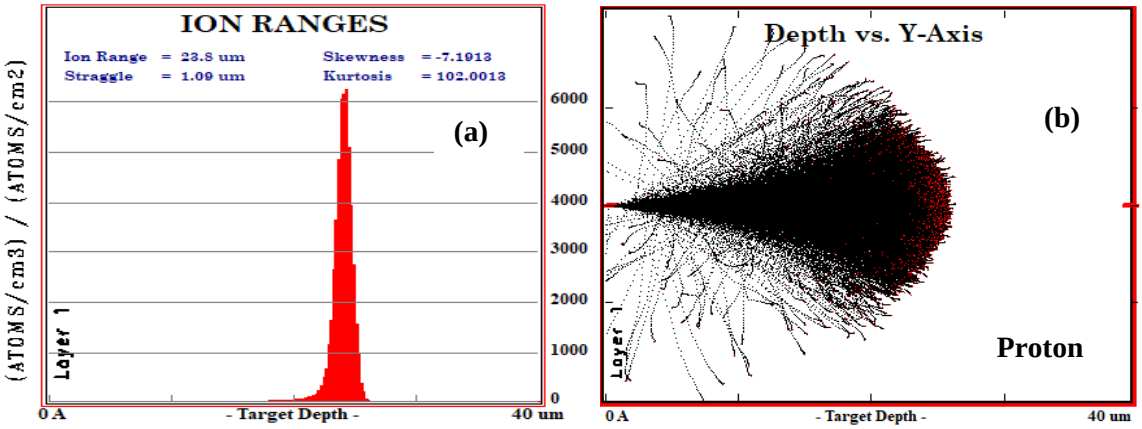

Fig. 12 The SRIM simulation of **(a)** range and **(b)** trajectories, for 2 MeV protons inside a G-metal alloy specimen

4 Conclusions

The G-metal alloy specimens were irradiated using 2 MeV Au^+ beam with different fluences. The microstructure, nanoindentation hardness, surface roughness, and elemental analysis of specimens surface were all characterized. The XRD patterns revealed that the four noticeable planes namely (111), (200), (220), and (311) are associated with host Cu-metal and other diffracted peaks for Zn and Sn also exist. The Au^+ irradiation did not create any new XRD phase. The shift in FWHM and intensities of diffracting planes, however suggested structural disturbance in G-metal alloy lattice structure. Harris analysis shows that the preferable oriented planes are (111), (200), and (220) for un-irradiated specimen. The preferable orientation of the specimen is influenced by the ion irradiation fluence. The maximum peak intensity plane (111) is one of the preferable oriented plane for all irradiated specimens. The estimation of ion irradiated material surface hardening is difficult due to the low depth of ion-induced defects region. So, the technique of nanoindentation used in this work proves helpful for estimating the surface hardness values for ion irradiated material. The surface hardness value of specimens varied with the Au^+ fluence as well as indentation depth. When the Au^+ fluence was 5×10^{13} Au^+/cm^2, the surface roughness elastic modulus and hardness reached at their maximum value. Nanoindentation surface hardness also reflects the Hall Petch relation. FESEM micrographs revealed the creation of clusters and distinct circular agglomers upon irradiation. PIXE and EDX analysis identified the presence of the similar elements in specimen before and after irradiation.

References

[1] P. T. Craddock, "The composition of the copper alloys used by the Greek, Etruscan and Roman civilizations: 3. The origins and early use of brass," *Journal of Archaeological Science,* vol. 5, no. 1, pp. 1-16, 1978.

[2] E. Gliozzo, W. A. Kockelmann, and G. Artioli, "Neutron diffraction of Cu–Zn–Sn ternary alloys: Non-invasive assessment of the compositions of historical bronze/brass copper ternary alloys," *Journal of Applied Crystallography,* vol. 50, no. 1, pp. 49-60, 2017.

[3] S. Naeem *et al.*, "Laser surface hardening of gun metal alloys," *Materials,* vol. 12, no. 16, p. 2632, 2019.

[4] Z. Shang *et al.*, "He ion irradiation response of a gradient T91 steel," *Acta Materialia,* vol. 196, pp. 175-190, 2020.

[5] A. Xu, I. Susanto, T. Wei, M. Ionescu, J. Daniels, and D. Bhattacharyya, "Investigation of mechanical property changes in He2+ ion irradiated MA957 through nanoindentation and in situ micro-tensile testing," *Journal of Nuclear Materials,* vol. 547, p. 152819, 2021.

[6] H. Zhang, X. Zhang, Y. Li, P. Wang, and L. Qiao, "Effects of deuterium plasma exposure and helium ions irradiation on nanoindentation hardness of tungsten," *Nuclear Materials and Energy,* p. 101722, 2024.

[7] X. Zhang, X. Mei, Q. Zhang, X. Li, J. Qiang, and Y. Wang, "Damage induced by helium ion irradiation in Fe-based metallic glass," *Journal of Nuclear Materials,* vol. 490, pp. 216-225, 2017.

[8] O. A. Waseem and H. J. Ryu, "Helium ions irradiation analysis of W0. 5 (TaTiVCr) 0.5 for application as a future fusion plasma-facing material," *Materials Chemistry and Physics,* vol. 260, p. 124198, 2021.

[9] D. Ueyama *et al.*, "Modification of microstructure and hardness for Cu–Ti alloy by means of energetic ion beam irradiation," *Nuclear Instruments and Methods in Physics Research Section B: Beam Interactions with Materials and Atoms,* vol. 341, pp. 53-57, 2014.
[10] J. Zuo, Z. Wang, and E. Han, "The effect of ion irradiation on the tensile and fatigue properties of Ti–6Al–4V alloy," *Materials Science and Engineering: A,* vol. 527, no. 15, pp. 3396-3401, 2010.
[11] Y. Yang *et al.*, "Irradiation hardening of pure vanadium and vanadium alloys due to helium ion implantation and displacement damage," *Journal of Nuclear Materials,* vol. 540, p. 152381, 2020.
[12] S. Chae, Y.-S. Kim, and M. Rafique, "Spectroscopic and microstructural characterization of 18 MeV He+ ions irradiated pure Al," *Optik,* vol. 127, no. 20, pp. 9152-9160, 2016.
[13] M. A. Chowdhury, U. K. Debnath, D. M. Nuruzzaman, and M. M. Islam, "Experimental evaluation of erosion of gunmetal under asymmetrical shaped sand particle," *Advances in Tribology,* vol. 2015, no. 1, p. 815179, 2015.
[14] X. Li and B. Bhushan, "A review of nanoindentation continuous stiffness measurement technique and its applications," *Materials characterization,* vol. 48, no. 1, pp. 11-36, 2002.
[15] D.-H. Lee *et al.*, "A novel methodology to estimate hydrogen diffusivity and its applications in revealing hydrogen effects in CoCrNi medium-entropy alloy versus 316L stainless steel," *International Journal of Plasticity,* vol. 169, p. 103737, 2023.
[16] B. Lucas and W. Oliver, "Indentation power-law creep of high-purity indium," *Metallurgical and materials Transactions A,* vol. 30, pp. 601-610, 1999.
[17] Y. Zhao, I.-C. Choi, Y.-J. Kim, and J.-i. Jang, "On the nanomechanical characteristics of thermally-treated alloy 690: Grain boundaries versus grain interior," *Journal of alloys and compounds,* vol. 582, pp. 141-145, 2014.
[18] M. Jandaghi, P. Parvin, M. Torkamany, and J. Sabbaghzadeh, "Alloying elemental change of SS-316 and Al-5754 during laser welding using real time laser induced breakdown spectroscopy (LIBS) accompanied by EDX and PIXE microanalysis," *Physics Procedia,* vol. 5, pp. 107-114, 2010.
[19] A. Zucchiatti *et al.*, "Prehispanic goldwork technology study by PIXE analysis," *Nuclear Instruments and Methods in Physics Research Section B: Beam Interactions with Materials and Atoms,* vol. 332, pp. 160-164, 2014.
[20] R. E. Stoller, M. B. Toloczko, G. S. Was, A. G. Certain, S. Dwaraknath, and F. A. Garner, "On the use of SRIM for computing radiation damage exposure," *Nuclear instruments and methods in physics research section B: beam interactions with materials and atoms,* vol. 310, pp. 75-80, 2013.
[21] M. Butt, D. Ali, M. Aftab, F. Bashir, M. Khalid, and M. Khaliq, "Role of carbon ions implantation in modifying the structural, electrical, and mechanical properties of W–8.57 Ni–6.34 Cu–1.34 Mo alloy," *Physica B: Condensed Matter,* vol. 573, pp. 49-61, 2019.
[22] M. Kumar, A. Kumar, and A. Abhyankar, "Influence of texture coefficient on surface morphology and sensing properties of W-doped nanocrystalline tin oxide thin films," *ACS applied materials & interfaces,* vol. 7, no. 6, pp. 3571-3580, 2015.
[23] Y. Wang, W. Tang, and L. Zhang, "Crystalline size effects on texture coefficient, electrical and optical properties of sputter-deposited Ga-doped ZnO thin films," *Journal of Materials Science & Technology,* vol. 31, no. 2, pp. 175-181, 2015.
[24] M. Scarisoreanu *et al.*, "Direct nanocrystallite size investigation in microstrained mixed phase TiO2 nanoparticles by PCA of Raman spectra," *Applied Surface Science,* vol. 470, pp. 507-519, 2019.
[25] M. Basak, M. L. Rahman, M. F. Ahmed, B. Biswas, and N. Sharmin, "The use of X-ray diffraction peak profile analysis to determine the structural parameters of cobalt ferrite nanoparticles using Debye-Scherrer, Williamson-Hall, Halder-Wagner and Size-strain plot: Different precipitating agent approach," *Journal of Alloys and Compounds,* vol. 895, p. 162694, 2022.
[26] C. D. Hardie, S. G. Roberts, and A. J. Bushby, "Understanding the effects of ion irradiation using nanoindentation techniques," *Journal of Nuclear Materials,* vol. 462, pp. 391-401, 2015.

[27] H.-S. Kim *et al.*, "A novel way to estimate the nanoindentation hardness of only-irradiated layer and its application to ion irradiated Fe-12Cr alloy," *Journal of Nuclear Materials,* vol. 487, pp. 343-347, 2017.

[28] B. Sulik *et al.*, "Fermi-shuttle acceleration of electrons in ion–matter interaction," *Nuclear Instruments and Methods in Physics Research Section B: Beam Interactions with Materials and Atoms,* vol. 212, pp. 32-44, 2003.

[29] M. A. Ali *et al.*, "3 MeV proton irradiation effects on surface, structural, field emission and electrical properties of brass," *Nuclear Instruments and Methods in Physics Research Section B: Beam Interactions with Materials and Atoms,* vol. 423, pp. 7-15, 2018.

[30] V. Popok, A. Stepanov, and V. Odzhaev, "Synthesis of silver nanoparticles by the ion implantation method and investigation of their optical properties," *Journal of Applied Spectroscopy,* vol. 72, pp. 229-234, 2005.

[31] N. Afzal, M. Devarajan, and K. Ibrahim, "Post-deposition annealing of magnetron sputtered InAlN film at different temperatures," *Journal of Alloys and Compounds,* vol. 640, pp. 260-266, 2015.

[32] M. Rafique, S. Chae, and Y.-S. Kim, "Surface, structural and tensile properties of proton beam irradiated zirconium," *Nuclear Instruments and Methods in Physics Research section B: Beam Interactions with Materials and Atoms,* vol. 368, pp. 120-128, 2016.

[33] K. Barfoot, I. Mitchell, L. Avaldi, H. Eschbach, and W. Gilboy, "Si (Li) detector efficiency below 10 keV," *Nuclear Instruments and Methods in Physics Research Section B: Beam Interactions with Materials and Atoms,* vol. 5, no. 3, pp. 534-544, 1984.

[34] S. F. Barros, N. L. Maidana, J. M. Fernández-Varea, and V. R. Vanin, "Full-energy peak efficiency of Si drift and Si (Li) detectors for photons with energies above the Si K binding energy," *X-Ray Spectrometry,* vol. 46, no. 1, pp. 34-43, 2017.

[35] N. Carmona, I. Ortega-Feliu, B. Gómez-Tubío, and M. Villegas, "Advantages and disadvantages of PIXE/PIGE, XRF and EDX spectrometries applied to archaeometric characterisation of glasses," *Materials Characterization,* vol. 61, no. 2, pp. 257-267, 2010.

[36] W. Kwiatek, B. Kubica, C. Paluszkiewicz, and M. Gałka, "Trace element analysis by means of synchrotron radiation, XRF, and PIXE: selection of sample preparation procedure," *Journal of alloys and compounds,* vol. 328, no. 1-2, pp. 283-288, 2001.

[37] F. Mirani *et al.*, "Integrated quantitative PIXE analysis and EDX spectroscopy using a laser-driven particle source," *Science advances,* vol. 7, no. 3, p. eabc8660, 2021.